

# A Self-Decoupled 32 Channel Receive Array for Human Brain Magnetic Resonance Imaging at 10.5T

Nader Tavaf<sup>1</sup>, Russell L. Lagore<sup>1</sup>, Steve Jungst<sup>1</sup>, Shajan Gunamony<sup>2</sup>, Jerahmie Radder<sup>1</sup>, Andrea Grant<sup>1</sup>, Steen Moeller<sup>1</sup>, Edward Auerbach<sup>1</sup>, Kamil Ugurbil<sup>1</sup>, Gregor Adriany<sup>1</sup>, Pierre-Francois Van de Moortele<sup>1</sup>

<sup>1</sup> Center for Magnetic Resonance Research (CMRR), University of Minnesota, Minneapolis, MN

<sup>2</sup> Centre for Cognitive Neuroimaging, University of Glasgow, Glasgow, Scotland

\* Correspondence: Nader Tavaf, Email: tavaf001@umn.edu

**Purpose:** Receive array layout, noise mitigation and  $B_0$  field strength are crucial contributors to signal-to-noise ratio (SNR) and parallel imaging performance. Here, we investigate SNR and parallel imaging gains at 10.5Tesla (T) compared to 7T using 32-channel receive arrays at both fields.

**Methods:** A self-decoupled 32-channel receive array for human brain imaging at 10.5T (10.5T-32Rx), consisting of 31 loops and one cloverleaf element, was co-designed and built in tandem with a 16-channel dual-row loop transmitter. Novel receive array design and self-decoupling techniques were implemented. Parallel imaging performance, in terms of SNR and noise amplification (g-factor), of the 10.5T-32Rx was compared to the performance of an industry-standard 32-channel receiver at 7T (7T-32Rx) via experimental measurements using a human head shaped phantom.

**Results:** The 10.5T-32Rx provided 67% more central SNR and 87% more peripheral SNR compared to the 7T-32Rx. Minimum inverse g-factor value of the 10.5T-32Rx ( $\min(1/g) = 0.56$ ) was 51% higher than that of the 7T-32Rx ( $\min(1/g) = 0.37$ ) with  $R=4 \times 4$  2D acceleration, resulting in significantly enhanced parallel imaging performance at 10.5T compared to 7T. The g-factor values of 10.5T-32Rx were on par with those of a 64-channel receiver at 7T, e.g. 1.8 versus 1.9, respectively, with  $R=4 \times 4$  axial acceleration.

**Conclusion:** Experimental measurements demonstrated effective self-decoupling of the receive array as well as substantial gains in SNR and parallel imaging performance at 10.5T compared to 7T.

**Keywords:**

RF coils, self-decoupling, receive array, parallel imaging, ultra-high field MRI, noise correlation.

## 1. INTRODUCTION

Ultra-high field (UHF) magnetic resonance imaging (MRI) advantages, including higher image resolution, reduced acquisition time, and better signal-to-noise ratio (SNR), have opened new opportunities for advancement of various clinical and research projects<sup>1</sup>. For instance, applications of primary interest, which depend on UHF MRI to achieve high resolution whole brain coverage, include functional MRI (fMRI) studies<sup>2-4</sup>, brain connectivity mapping using diffusion-weighted imaging (DWI)<sup>5-7</sup>, as well as neuroimaging<sup>8-11</sup> and anatomical images<sup>12-14</sup>.

The push for UHF MRI is predicated primarily on the premise of significant ultimate intrinsic SNR<sup>15,16</sup> gains and acceleration with less SNR penalty at higher  $B_0$  field strengths<sup>14,17-19</sup>. Although the push to UHF MRI presents significant technical challenges<sup>1,2,20-23</sup>, abovementioned UHF advantages can potentially be materialized via parallel imaging<sup>19</sup> using high density receive arrays<sup>24-26</sup>.

Acceleration via parallel imaging comes with a penalty in SNR quantified in terms of noise amplification or g-factor<sup>27</sup>. Increasing the  $B_0$  field strength has been shown to mitigate the SNR penalty attributed to acceleration<sup>19,28</sup>, hence affording better parallel imaging performance. However, parallel imaging performance depends significantly on receiver array noise correlation<sup>29,30</sup> as well. Increasing receive array density, on the other hand, exacerbates interelement coupling (noise correlation) and

electronics noise dominance of smaller loops<sup>24,31,32</sup>. Moving to higher  $B_0$  field accentuates the noise correlation challenge via reducing electromagnetic wavelength and attenuates the electronics noise dominance challenge via increasing coil coupling into the sample<sup>24,33,34</sup>. Hence, novel receive array decoupling methods had to be developed to capture SNR gains at ultra-high frequencies. In other words, for two receive arrays with equal channel count, one for 7T and another for 10.5T, it was imperative to implement novel decoupling techniques for the receiver operating at higher frequency to fully exploit the superior SNR and acceleration potential of the higher magnetic field<sup>25</sup>.

Various Radio Frequency (RF) array decoupling strategies have been proposed and implemented in the past. Overlap and preamplifier decoupling proposed by Roemer et al.<sup>35</sup> have been improved and used extensively in designs of high density receive arrays<sup>32,33,36-39</sup>. Noise matching the preamplifiers<sup>24,33</sup> and inductive decoupling<sup>36</sup> were also heavily relied upon in previous works. Furthermore, self-decoupling techniques for low density (up to 8-channels) transmit arrays using intentionally unbalanced capacitive distribution were proposed<sup>40,41</sup>. Lakshmanan et al.<sup>41</sup> proposed the loopole antenna, where segmenting capacitors inside transceiver loops were distributed unevenly to cause an unbalanced current distribution in the loop with electromagnetic field patterns resembling that of a dipole antenna. Yan et al.<sup>40</sup> built on the idea of unbalanced impedances and proposed a transceiver self-decoupling scheme for 7T / 298MHz where a relatively small RF impedance (e.g. 8.5pF capacitance) is placed opposite a relatively large RF impedance (e.g. 0.4pF) which approaches an open circuit at the RF frequency. This results in the current distribution being unbalanced so that the coil resembles a dipole antenna. However, in contrast to Roemer's work<sup>35</sup>, Yan's analysis assumes electric coupling to be limited to coupling via free space and excludes resistive coupling via the conductive sample. While inter-element coupling via the sample can be negligible in the case of loop transmitters far (more than 4cm away) from the sample, 3D conformal receiver arrays are generally form-fitting and very close to the sample and are designed to be dominated by body noise<sup>24,25,31</sup>. In this work, we present a strategy for receiver self-decoupling at 447MHz based on our observation that higher frequencies allow for a more balanced capacitive segmentation of receive elements while maintaining acceptable decoupling. We compare performance of self-decoupled receivers, in terms of SNR, with overlap-decoupled loops. Receiver self-decoupling provides inter-element isolation comparable to overlap decoupling while it does not require geometric overlap or interelement transformers or decoupling networks and is therefore much more practical to implement in high density receive arrays. Furthermore, we show that receiver self-decoupling presented here provides higher SNR compared to overlap decoupling.

Here, we implement the novel receiver self-decoupling technique and build a high density, self-decoupled 32-channel receive array for 10.5T/447MHz for the first time, without using within-row (axial) overlap<sup>35</sup>, explicit inter-element decoupling networks<sup>36,42,43</sup>, or unbalanced current distributions<sup>40,41</sup>, with preliminary results reported in an ISMRM abstract<sup>44</sup>. The self-decoupled 32-channel receive array (10.5T-32Rx) provided substantial experimental cortical and central SNR gains compared to an industry-standard 32-channel receive array at 7T. Furthermore, parallel imaging performance at the 10.5T was superior to that of the 7T, with 10.5T-32Rx providing acceleration performance comparable to a 64-channel receiver at 7T.

## 2. METHODS

### 2.1. 16-Channel Transmitter

The primary focus of this paper is on the contribution of receiver technology and  $B_0$  field strength to SNR and parallel imaging performance. Therefore, the transmitter design is covered here only briefly, with

its meticulous characterization published separately<sup>45</sup>. A 16-channel transmitter comprising two rows of 8 inductively decoupled rectangular loops was used<sup>37,45</sup>. The 2-row design of the transmitter array has the potential of increasing degrees of freedom in parallel transmit (pTx) RF pulse design especially for specific absorption rate (SAR) control. In order to minimize transmit-receive interaction, the transmitter was actively tuned, i.e. a PIN diode circuitry was used to tune the transmitter during signal transmission, leaving it off-resonance during reception. The procedure to obtain necessary approvals for in-vivo human brain imaging using this transmitter is currently ongoing.

## 2.2. Receiver Self-Decoupling

Rectangular loops similar in size to those used in the array were modeled in several scenarios. First, two  $5 \times 5 \text{cm}^2$  loops and then, two  $2.5 \times 5 \text{cm}^2$  were positioned on a flat surface in proximity to a cubic phantom (permittivity  $\epsilon_r = 50$ , conductivity  $\sigma = 0.6 \text{S/m}$  to approximate human brain tissue properties<sup>46</sup> across all simulations). These loops were constructed using AWG-18 copper wire (circular cross section, diameter 1.02mm) and were divided into four segments using three capacitors and the feed point. Two fixed capacitors and a trimmer capacitor ( $X_{tr}$ ), with values in the same range as fixed capacitors, were used inside each loop. The feed circuitry, presented in Figure 1c, consisted of a detune trap as well as tune ( $X_t$ ) and match ( $X_m$ ) adjustable capacitors. Similar principles were used to construct non-overlapped  $10 \times 10 \text{cm}^2$  loops using balanced capacitive distribution on a cylindrical surface at a constant distance from a cylindrical sample ( $\epsilon_r = 50$ ,  $\sigma = 0.6 \text{S/m}$ ) as shown in Figure 2b.

Electromagnetic/circuit co-simulations were performed using CST Studio (Dassault Systèmes Simulia Corp., Johnston, RI). Coil elements were modeled in SolidWorks (SolidWorks Corp., Waltham, MA) and imported into CST. Simulations were performed over a frequency range of 2GHz using the finite-difference time-domain method to solve Maxwell's equations and were partially accelerated using a GPU. The loops were tuned to 447MHz (proton resonance at 10.5T) and matched to 50Ohm. The simulation pipeline has been discussed in more detail in previous works<sup>45</sup>.

Several electromagnetic (EM)/circuit optimization problems were set up with the goal of finding  $X_{tr}, X_t, X_m$  to minimize  $S_{21,f}$  conditioned on  $S_{11,f} \leq -12 \text{dB}$  and  $S_{22,f} \leq -12 \text{dB}$  where  $f = 447 \text{MHz}$  is the resonant frequency. Values of  $X_{tr}, X_t, X_m$  were limited to practical ranges guided by bench experiment. Other 3D EM model parameters, including the distance between loop elements and the gap between the coils and the phantom were kept constant and equal to practical receive array values during optimization. Note that the objective function and the cost (loss) function for these optimizations can be defined in various ways. In our experience, incorporating the objective ( $S_{21,f}$ ) into the loss function to form a weighted-linear combination of individual L1 norms in the linear (as opposed to dB) scale of real and imaginary parts of the S-parameters resulted in faster convergence. The trust region method and the Nelder Mead simplex algorithm were used to solve for optimums. It should be noted that in practice (on the bench) such an optimization is straight-forward and is substantially less time consuming compared to numerical simulations because on the bench, the results of parameter modifications can be monitored immediately in an analogue manner using a vector network analyzer.

Numerical results for S-parameters and per-port, complex-valued H-fields at 447MHz were exported to ASCII files. Post-processing and analysis of magnetic field results were performed using customized Python scripts. Complex-valued receive magnetic fields were calculated for each coil element using  $B_1^- = \mu_0 (H_x^* + jH_y^*)/2$  where  $\mu_0$  is the permeability of free space and  $x, y$  are Cartesian coordinates orthogonal to the static magnetic field ( $B_0$ ). In order to compare the receive field between overlap and self-decoupling methods, two metrics were calculated: sum of magnitude (SOM) of the complex combined magnetic fields

SOM =  $\sum_{\text{sample}} |\sum_{\text{channels}} B_1^-|$  and the root sum of squares (RSOS) of magnitudes of each channel's magnetic field  $RSOS = \sum_{\text{sample}} \sqrt{(\sum_{\text{channels}} |B_1^-|^2)}$ , in other words  $RSOS = \sum_{\text{sample}} \sqrt{B^H B}$  where  $B$  is a vector composed of complex magnetic receive fields of each individual channel and  $H$  is Hermitian transpose. Furthermore, RSOS was corrected for noise correlation to calculate noise-correlation-weighted SNR as given by  $SNR = \sum_{\text{sample}} \sqrt{B^H \psi^{-1} B}$  where  $\psi$  is the normalized noise correlation matrix calculated using the simulated complex-valued scatter matrix<sup>24,47-50</sup>. The summation over sample is intended to collapse spatial maps into a single numeric metric for comparison purposes. These metrics are particularly appropriate here as we are considering receive-only coils, so we are interested in SNR, not transmit efficiency.

### 2.3. 32-Channel Receiver

A close-fitting receive former (helmet) was designed while considering physical constraints imposed by the transmitter, the dimensions of which are directed by a head gradient coil that will be used in the future. The shape of the former was optimized based on previous helmet designs, numerical model of a human head, and consideration of average range of head sizes. A structure for mechanical support of the preamplifiers and cables was designed to be mounted as an additional part on top of the head former. The receive visual channel at the eyes' level was designed to be compatible with the needs of future cognitive studies (e.g. involving visual stimulus presentation or eye tracking). The distribution of preamplifier substrates was driven by cable routing design, which will be discussed subsequently, as well as preamplifier interactions and directional sensitivity compared to the static magnetic  $B_0$  direction.

The 32Rx receive array is composed of 31 loops, divided into four rows along the z-axis, and one cloverleaf element covering the top. The layout of the loops, presented in Figure 1a, allowed for partial overlap among rows (8-10mm) and gaps between neighboring loops in each row (5-8mm) as self-decoupled loops with gaps in the axial (x-y) plane are shown here to provide an SNR advantage compared to overlapped loops (see Table 1). This results in a high-density receive array designed to rely primarily on self-decoupling. Each row of loop elements was shifted (by a half loop) compared to the neighboring rows. This self-decoupled design reduced construction complexity that would arise from overlapping adjacent loops within each row or using decoupling networks or transformers between loop elements and contributed to the SNR improvements. Overlap along the z-axis (along the center of the MR scanner bore) was maintained to further improve SNR via increased channel density. A key consideration in designing the layout was a primary focus on the visual cortex, driven by a large array of vision neuroscience projects conducted at CMRR that can greatly benefit from higher field strength; this, in turn, motivated an increase in density in the posterior array for the rows that will be facing the occipital lobe, at the expense of a reduced density at the top (six loops) and bottom (three loops) rows. As aligning a loop plane perpendicularly to the z-axis would compromise its sensitivity, a cloverleaf element, rather than loop elements, was placed at the top of the coil, resulting in a poynting vector perpendicular to the z-axis. The cloverleaf element was composed of two perpendicular loops, each with crossed-over legs, whose outputs were combined into a single receive channel.

A prototype composed of eight channels, arranged in four rows to be representative of the final layout, was initially built and tested on the bench prior to measurements in a head shaped gel phantom at 10.5T. An American Wire Gauge AWG-16 silver-coated wire was used to construct the loops. Lumped capacitor values used in the loops were 3.3pF, 4.7pF, and 6.8pF. One trimmer capacitor with a value range of 8-20pF or 2-6pF (SGC3S300NM or SGC3S060NM, Sprague-Goodman, NY, USA), included inside each loop,

was carefully adjusted to decouple the loops in each row based on their scatter matrix parameters. The values of the larger trimmers were measured to be in the range of 8.5-15pF after adjustment. The feed board, including the active detuning circuitry, and the preamplifier board were similar to those presented in a previous ISMRM abstract<sup>51</sup>.

#### 2.4. Receiver Noise Correlation Mitigation

On the bench, the scatter matrix ( $S_{ij}$ ) was measured between all coil pairs using the 8-channel prototype. Similar  $S_{ij}$  measurements for the completed 32-channel array were limited to adjacent coils in the same row or overlapping coils from different rows, considered to represent worst-case scenarios. Measurements were done after tuning, matching, and self-decoupling the coils and both prior to and after adding preamplifiers. Self-decoupling of adjacent loops within each row provided robust inter-element isolation. Low noise preamplifiers (WMA447A, WanTcom Inc., Minneapolis, MN) with input impedance of  $1.5\Omega$  and noise figure of 0.45dB were used for preamplifier decoupling. Preamplifiers were mounted on a ground plane which helped minimize interactions with transmitter/receiver elements and preamp oscillations. To reflect the actual use case,  $S_{ij}$  measurements were done with all receive elements in the tuned state.

Preamplifier interactions and coaxial cable interactions were investigated to characterize the effects of stacking preamps/coaxial cables close to each other as well as cable routing. Noise correlation matrices for various cabling, preamplifier configurations, and cable trap locations were measured inside the 10.5T MR scanner with the 8-channel prototype and a head shaped phantom. Coaxial cables were isolated using self-shielded input cable traps to suppress shield-current-induced noise<sup>52,53</sup>. Traps were carefully tuned after being installed on preamplifier input coaxial cables; however, several cable traps were intentionally tuned slightly off-resonance to mitigate their interaction with resonant loops of the receiver or transmitter<sup>37</sup>. These input cable traps were constructed via resonating a trimmer capacitor (8-30pF, SGC3S300NM, Sprague-Goodman, NY, USA) with copper tape soldered to the outer conductor of preamp input coaxials. One further s-matrix measurement was made with output cable traps detuned to investigate potential crosstalk between those resonant structures as well.

#### 2.5. Transmit-Receive Interaction

Design of routing paths for preamplifier input coaxial cables was driven by noise correlation and receive-transmit interaction considerations. Coaxial cables may present a significant conductor barrier to the transmitter. Coaxial cables longer than  $1/10^{\text{th}}$  wavelength (6.7cm at 10.5T) have considerable electromagnetic interaction, significantly distorting transmit magnetic field ( $B_1^+$ ) and adversely affecting the receive array noise correlation matrix. At 7T, or 298MHz,  $1/10^{\text{th}}$  of the wavelength is 10cm; as such, input coaxial cables (8-9cm) would not be as electromagnetically problematic as they are at 10.5T. Based on previous experience with loop transmitter designs<sup>36</sup>, knowledge of transmit field patterns<sup>45</sup>, and prototype experiments explained above, it was determined that collecting coaxial cables in five paths along the z-axis parallel to the center of the transmit loops would result in minimum Tx/Rx interaction.

Measurements of the receive-transmit interaction were performed both on the bench and in the scanner. On the bench, scatter matrix parameters of the transmitter were monitored before, during, and after insertion of the receive array, while the receiver was actively detuned using DC supply to PIN diodes<sup>51</sup> and loaded with a human head shaped phantom. In the scanner, transmit field maps were acquired in two configurations: first, with the 16-channel transmitter and 32-channel receiver as an ensemble transmit-only receive-only coil, second, with the 16-channel transmitter used as a transceiver in the absence of the 32-

channel receiver. Relative transmit  $B_1^+$  maps were acquired using a small flip angle multi-slice gradient echo (GRE) sequence with magnitude images from sequential single channel transmissions normalized by their sum<sup>54</sup>. Absolute transmit  $B_1^+$  maps were then generated by normalizing relative transmit maps by  $\sin(\alpha(\vec{r}))$  where  $\alpha(\vec{r})$  is actual flip angle as a function of spatial coordinate ( $\vec{r}$ ) obtained via 3D GRE Actual Flip Angle (AFI) acquisitions<sup>55,56</sup>. Absolute transmit field maps were acquired both with and without the receive array in place, with the transmitter used as a transceiver when the 32-channel receive array was not inserted.

## 2.6. SNR and g-Factor

### *Data acquisition*

All data were acquired on a 10.5T MRI (Siemens Healthcare, Erlangen, Germany) system using human head shaped gel phantoms (with permittivity  $\epsilon_r \approx 50$ , conductivity  $\sigma \approx 0.6\text{S/m}$  as measured with dielectric probe to approximate human brain tissue properties<sup>46</sup>). All SNR measurements were replicated two times, once with the 16Tx/32Rx coil described above at 10.5T, then with an industry-standard 1Tx/32Rx coil (Nova Medical Inc., Wilmington, MA) at 7T using protocols, acquisition parameters, setups, and data analysis pipelines similar to those at 10.5T.

Relative transmit field maps were obtained using a series of small flip angle multi-slice gradient echo (2D GRE) sequences, pulsing on one transmit channel at a time<sup>57,58</sup>. Typical sequence parameters were seven 5 mm thick axial slices (with center slice being isocenter), TR=100ms, TE=3.5ms, FA=10°, pixel bandwidth = 300 Hz/pixel. Actual flip angle (AFI)<sup>56</sup> maps were acquired (3D, TR=75ms, TE=2.0ms, nominal FA=50°) with all channel transmitting together. Individual channel transmit field maps were derived from both acquisitions. SNR data were acquired in an approximately full longitudinal relaxation state, with a multi-slice GRE sequence in the same 7 axial slices used for B1 mapping, with TR=7000ms-10000ms, TE=3.5ms, FA=80°, pixel bandwidth = 300 Hz/pixel. This was followed by a *noise* scan which was identical to the SNR sequence except for FA=0° (no RF pulse), TR=70-100ms<sup>59</sup>. For the 10.5T 16Tx, circularly polarized (CP-like) transmit field  $B_1^+$  phase shim setting were calculated with an efficiency-homogeneity trade-off as the objective, allowing for acceptable  $B_1^+$  efficiency at the center<sup>23,60</sup>. The same resulting 16-channel  $B_1^+$  shim setting was used in all acquisitions.

### *SNR and g-factor calculations*

The noise correlation matrix was calculated based on complex noise data (obtained in the absence of RF pulsing) and used to decorrelate the SNR data before they were combined using root sum-of-square method<sup>35,48</sup>. In steady state gradient echo, signal intensity is proportional to  $\rho(1 - E_1)(\sin \theta)/(1 - E_1 \cos \theta)E_2$  where  $\rho$  represents proton density,  $E_1 = \exp(-T_R/T_1)$ ,  $E_2 = \exp(-T_E/T_2^*)$  and  $\theta$  is the spatially varying, voltage-normalized actual flip angle map. With  $T_R \gg T_1$  it follows that  $E_1 \ll 1$  which results in  $SNR \propto \rho \sin(\theta) E_2$  where  $\sin(\theta)$  is the flip angle distribution reflecting transmit  $B_1^+$  inhomogeneity. SNR maps were normalized by  $\sin(\theta)$ , voxel size, number of acquisitions, number of samples along the read-out and phase-encoding directions, and bandwidth to make SNR calculations comparable across experiments<sup>55</sup>.  $T_2^*$  decay and the noise figure from receiver chain of the MR scanners (excluding RF coil and preamplifiers) were not reflected in these calculations. Noise amplification in accelerated images was quantified in terms of g-factor<sup>27</sup> and calculated as  $g = SNR / (SNR_R \times \sqrt{R})$  where R is the acceleration factor and  $SNR_R$  is the accelerated SNR calculated based on fully sampled acquisitions retrospectively under-sampled. In order to be able to compare g-factor numbers of the 10.5-32Rx presented here with previously published<sup>13</sup> g-factors of 7T-32Rx and 7T-64Rx, the same acquisition and post-

processing pipeline used for 7T-32Rx and 7T-64Rx were maintained in our experiments with the 10.5T-32Rx.

### 3. RESULTS

#### 3.1. Receiver Self-Decoupling

Figure 2(b-e) presents simulation results for two  $10 \times 10 \text{cm}^2$  receive loops at 10.5T/447MHz. The resulting crosstalk between receive elements is  $S_{21} = -12 \text{ dB} \approx 6$  percent which leads to the magnetic field of the second loop to be slightly visible in the  $B_1^-$  plot. However, this does not distort the field pattern of the excited loop, implying sufficient isolation. The surface current distribution is almost symmetric with strong current distributed on all segments of the excited loop (and negligible current induced on the second loop), again demonstrating sufficient interelement isolation

Simulation results for  $25 \times 50 \text{mm}^2$  receive loops demonstrated -11.2dB isolation using the self-decoupling method (compared to -13.8dB using overlap) at 447MHz. In the case of  $50 \times 50 \text{mm}^2$  loops, self-decoupling provided  $S_{21} = -12.9 \text{dB}$  interelement isolation (compared to -16.8dB using overlap). These results indicate that the proposed self-decoupling method achieves better than -11dB isolation (in the worst-case scenario) which is sufficient for receive array design given that preamplifier decoupling will further improve the isolation.

Figure 3 depicts the receive magnetic fields ( $B_1^-$ ) resulting from self-decoupled loops and provides a qualitative comparison with  $B_1^-$  from overlapped loops. The RSOS combination of receive signals from self-decoupled loops shows strong receive signal despite the gap between the two loops. Table 1 presents a quantitative comparison between SOM, RSOS and SNR of self-decoupled and overlapped loops for two sets of loop sizes. Compared to overlapped loops, the proposed self-decoupling method provides 17% more RSOS  $B_1^-$  for the  $25 \times 50 \text{mm}^2$  loops and 32% more RSOS  $B_1^-$  for the  $50 \times 50 \text{mm}^2$  loops. Furthermore, self-decoupling results in 10% and 26% higher noise-correlation-weighted SNR for  $25 \times 50 \text{mm}^2$  and  $50 \times 50 \text{mm}^2$  loops, respectively.

#### 3.2. Receiver Noise Correlation and Interaction with Transmit Field

The values of inter-element isolation measured prior to preamplifier decoupling in terms of  $S_{21}$  at the resonance frequency of 447MHz, using a 16-port vector network analyzer (VNA, ZNBT8, Rohde & Schwarz), corrected for 2dB cable loss, were in the range of 11-12dB for self-decoupled adjacent coils in the same row and 12-15dB for partially-overlapped coils from different rows (see Figure 2a), and in the range of 20-30dB negative for distant neighbors, demonstrating effective self-decoupling of the 32-channel receive array without the need for overlap in each row, explicit transformer decoupling, or unbalanced capacitive distribution. Preamplifier decoupling further improved crosstalk between receive array elements to 35-40dB negative.

The noise correlation matrix measured inside the 10.5T MR scanner resulted in maximum noise correlation of 0.37 (Figure 4), which is a significant improvement compared to previous works<sup>13</sup>. We attribute this to the novel self-decoupling technique, experimentally optimized cable routing (relative to transmit elements to minimize shield-current-induced noise and transmit field distortion) and cable trap locations (to minimize trap interference with receive element resonances).

Figure 5 shows power-normalized transmit field maps (in  $\mu T / \sqrt{W}$ ) measured in the 10.5T scanner using the 16-channel transmitter with and without insertion of the 32Rx receive array. These maps demonstrated less than 10% distortion of the transmit field upon inserting receive array; as such, characterizing the limited transmit field change following the insertion of the receive array. This

characterization allows for streamlining safety validation studies by obviating the need for inclusion of the receive array in electromagnetic simulations of specific absorption rate (SAR).

### 3.3. SNR and g-Factor

Figure 6 illustrates experimental unaccelerated SNR comparisons in seven axial slices obtained with identical protocol, experimental setups, and analysis pipeline using a 32-channel receiver at 7T (7T-32Rx) and a 32-channel receiver at 10.5T (10.5T-32Rx). This comparison resulted in 67% more central SNR and 84% more peripheral SNR obtained using the 10.5T-32Rx compared with the 7T-32Rx. This enhanced SNR is primarily due to higher static magnetic field  $B_0$  strength as well as noise mitigation and SNR advantages provided by the self-decoupling method (see Table 1).

Figure 7 provides unaccelerated 3D (axial, coronal, sagittal) SNR comparisons between 10.5T-32Rx and 7T-32Rx in the central slices. The SNR ratio maps presented in Figure 7 show local hot spots where 10.5T-32Rx SNR is 2-2.5 times the 7T-32Rx SNR. These posterior hot spots follow the anatomically guided design of the 10.5T-32Rx intended to provide an SNR boost at the visual cortex. Figure 8 provides a line plot of the SNR along the y-axis of the axial slice of Figure 7 demonstrating significant SNR gains at 10.5T.

The performance of the 10.5T-32Rx in 2D accelerated acquisitions can be compared with the 7T-32Rx in terms of g-factors (presented in Table 2). The mean inverse g-factor of the 10.5T-32Rx ( $1/g = 0.69$ ) is 18% more than mean inverse g-factor of the 7T-32Rx ( $1/g = 0.59$ ) for 4x4 acceleration. Taking both the unaccelerated SNR advantage and the lower acceleration penalty of 10.5T-32Rx into account, the 4x4 accelerated SNR of the 10.5T-32Rx is expected to be 89% more than the 4x4 accelerated SNR of 7T-32Rx.

## 4. DISCUSSION

Previous studies have shown the necessity of using high density receive arrays at ultra-high field (UHF) to approach ultimate intrinsic SNR<sup>15,25</sup> and capitalize on the acceleration potential of ultra-high field MRI. In accelerated imaging with k-space undersampling, SNR is penalized by noise amplification of the receive array parametrized by the g-factor<sup>27</sup>. Therefore, receiver noise mitigation strategies play a critical role in the accelerated imaging performance at UHF MRI.

Here, we scaled up a novel self-decoupling approach<sup>40</sup> to noise mitigation to build a 10.5T 32-channel receive array. The self-decoupling method presented by Yan et al.<sup>40</sup> introduced a promising new method for decoupling of high density receiver arrays. However, the method at 3T and 7T operating frequencies requires significantly unbalanced distributed capacitors or introduction of inductive circuit elements to achieve the desirable unbalanced current distributions. Our data confirms Yan et al.'s suggestion that in high-density, 3D conformal receive arrays, self-decoupling can be paired with preamplifier decoupling to improve inter-element isolation. Importantly we demonstrate that the combination of higher frequency (447MHz), smaller loop sizes appropriate for a 32-channel receiver and distributed inductance of such loops being in the range required for self-decoupling, can be exploited to achieve acceptable inter-element isolation with a more uniform capacitive distribution at 447MHz. The proposed method improves the root-sum-of-squares of magnitudes of receive fields substantially, and results in better noise-correlation-weighted SNR compared to overlapped decoupling. We implemented the self-decoupling method in a 3D conformal, high density 32-channel receive-only array for human brain imaging at 447MHz for the first time.

We anticipate that at extreme high frequencies (447MHz and higher) self-decoupling strategy will significantly simplify future high density receive array design and construction as it obviates practical



complexities of common decoupling techniques. Experimental noise correlation matrix demonstrated effective interelement receiver decoupling and suggest this array configuration has a promising potential for parallel imaging. The receive array is shown to result in limited transmit field distortion following receive array insertion. This will facilitate the electromagnetic simulation effort for specific absorption rate (SAR) and regulatory validation. Furthermore, limited receiver-transmitter interaction can enable an interchangeable coil setup where a single transmitter can be used with 32-channel, 64-channel, and 128-channel receivers.

Peripheral and central SNR gains presented here in comparison to 7T confirm the expected gains<sup>61</sup> for ultra-high field imaging<sup>62-65</sup> and are crucial to various high resolution clinical and research applications of UHF MRI<sup>2,8-11</sup>. SNR and g-factor improvements can be attributed to several factors. On top of the fundamental contributions of increased static magnetic field strength, the self-decoupling method employed in this receive array is shown here to enhance SNR as well. Careful receiver noise correlation management was consequential to improved parallel imaging performance. The g-factor of 2D accelerated imaging using the 10.5T 32-channel receiver presented here was on par with a 64-channel receiver at 7T.

This work is a significant milestone towards building 64-channel and 128-channel receiver arrays for human brain imaging at 10.5T. It is fully anticipated that scaling up to a 128-channel design will pose additional challenges in noise mitigation, preamplifier design and oscillations, and receiver-transmitter interactions. However, expected SNR and parallel imaging gains provide strong rationale and impetus to address such challenges.

## **5. CONCLUSIONS**

There is significant clinical and research interest in capitalizing on the acceleration and signal-to-noise ratio (SNR) potential of ultra-high field MRI. Here, we present the first self-decoupled 32-channel receive array (32Rx) and capture substantially superior SNR and parallel imaging performance using a 10.5T MRI system compared to a 7T MRI system. The 10.5T-32Rx provided significant peripheral and central SNR gains compared to an industry-standard 7T-32Rx, both in unaccelerated and 2D accelerated acquisitions. This achievement delivers the much-anticipated SNR boost in highly accelerated ultra-high field imaging required for further understanding of human brain function and connectivity.

## **ACKNOWLEDGMENT**

The authors acknowledge the constructive feedback of Myung Kyun Woo, Lance DelaBarre, Yigitcan Eryaman, and Matt Waks (all with Center for Magnetic Resonance Research, University of Minnesota Twin Cities, Minneapolis, MN 55455) and funding from NIH S10 RR029672, NIH U01EB025144, BTRC P41 EB015894, P30 NS076408, P41 EB027061 and NIH R34AG055178 grants.

**FIGURES & TABLES**

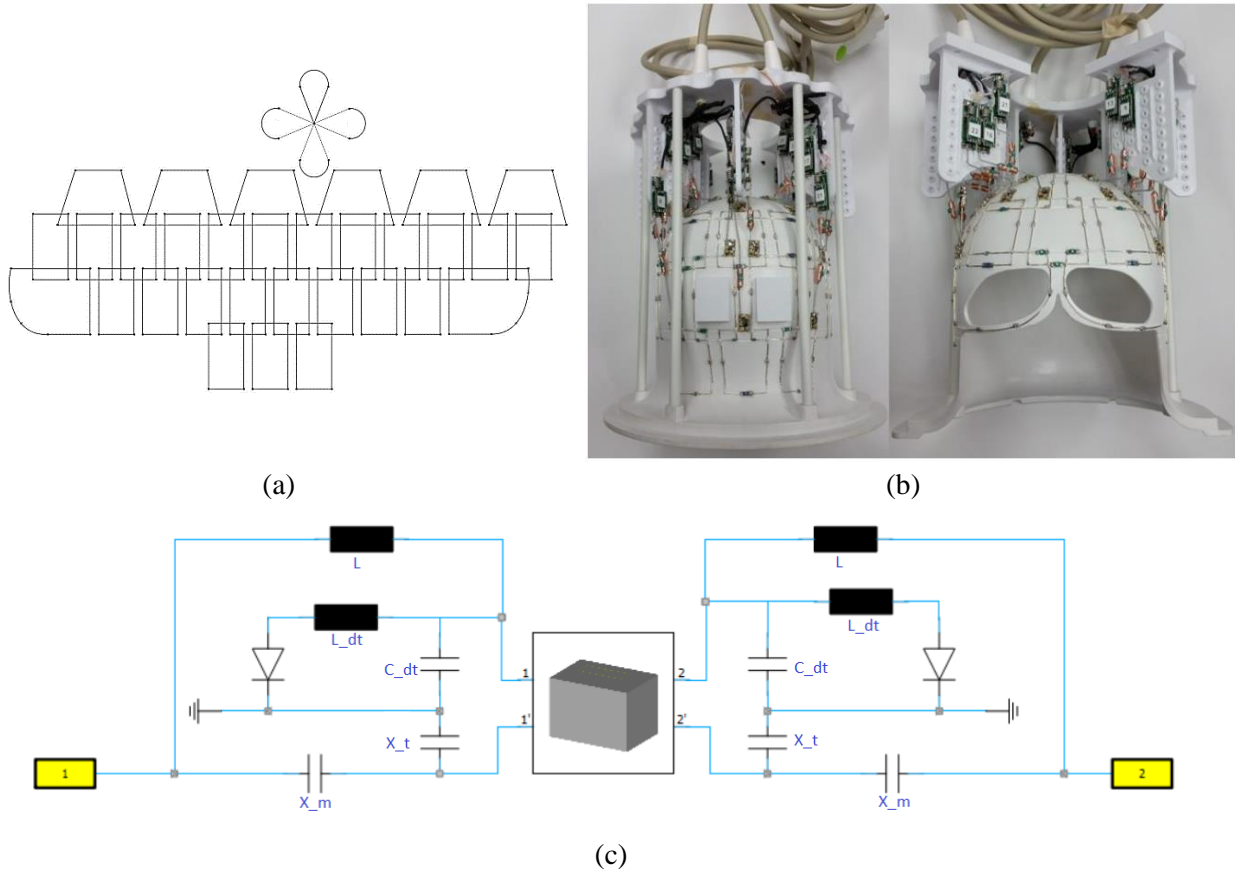


Figure 1 – The 10.5T 32-channel receive array, (a) flattened layout of the channels, (b) as-built image of the coil, (c) feed circuit (for two channels) consisting of tune ( $X_t$ ) and match ( $X_m$ ) capacitors as well as detune trap ( $L_{dt}$  and  $C_{dt}$ ). The trap is used to detune the receiver during transmit.

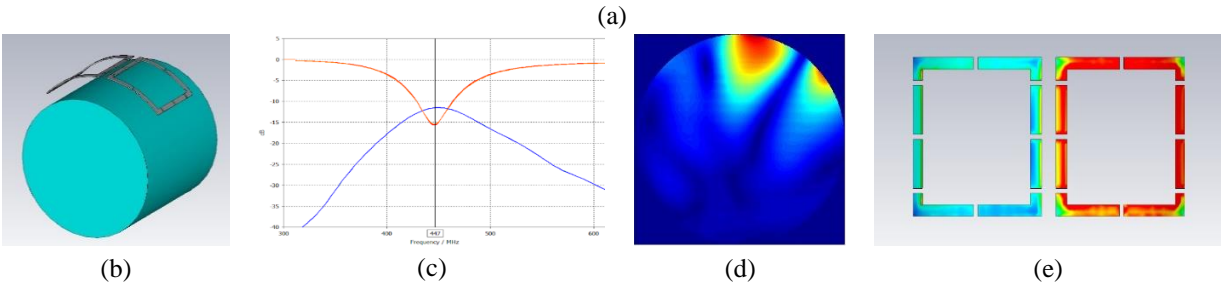
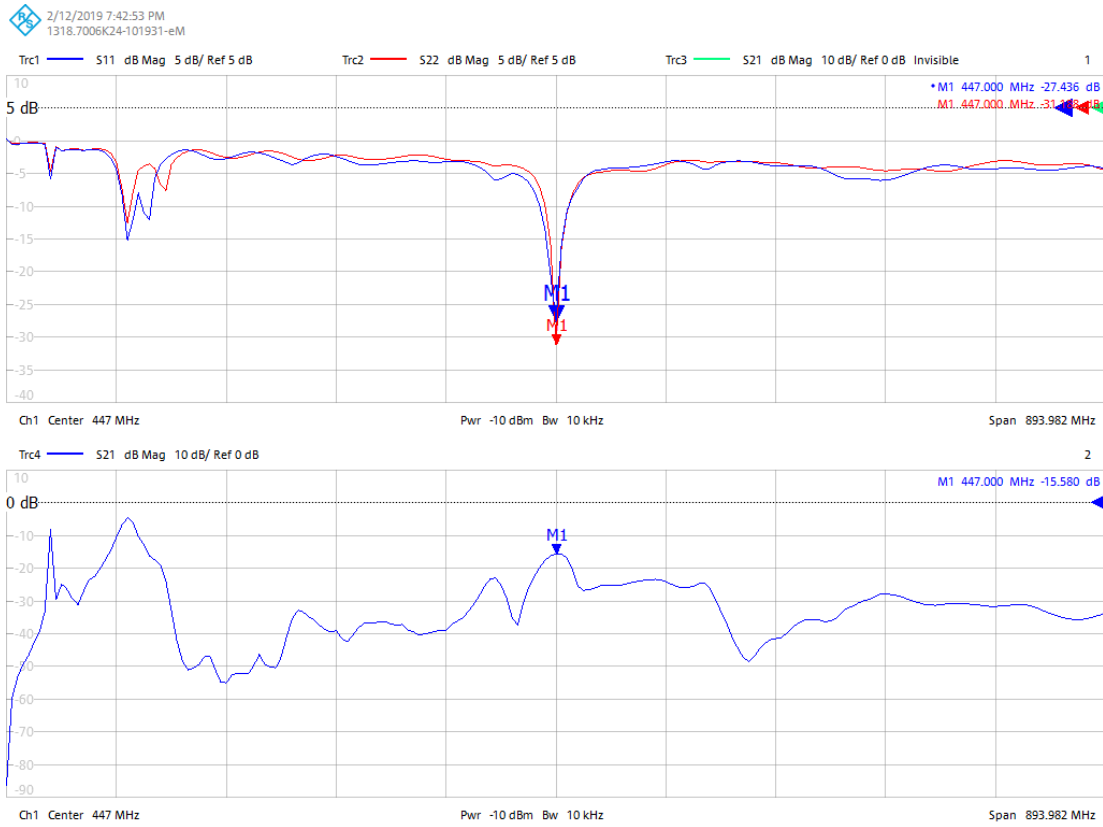


Figure 2 – (a) Experimental VNA screenshot demonstrating effective self-decoupling of adjacent loops with  $S_{11} = -27\text{dB}$ ,  $S_{22} = -31\text{dB}$ ,  $S_{21} = -15\text{dB}$  (including 2dB cable losses) at 447MHz; (b – e) Simulation results for two self-decoupled rectangular loops at  $10.5T/447\text{MHz}$ . (b) Electromagnetic model of the loops loaded at  $10.5T/447\text{MHz}$ , (c)  $S_{11}=S_{22} = -15\text{dB}$  (red) and  $S_{21} = -12\text{dB}$  (blue) at 447MHz, (d)  $B_{1+}$  transmit field of each loop (axial, center slice), (e) normalized current distribution.

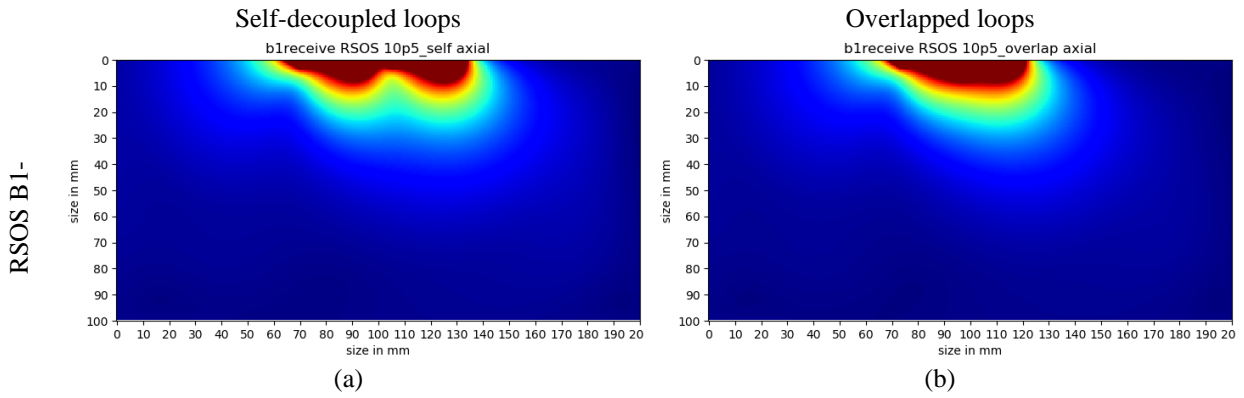


Figure 3. Normalized combined  $B_1^-$  receive fields for two rectangular  $25 \times 50 \text{ mm}^2$  loops, with (a) root-sum-of-squares (RSOS) of receive fields for self-decoupled, non-overlapped loops, and (b) RSOS for overlapped loops.

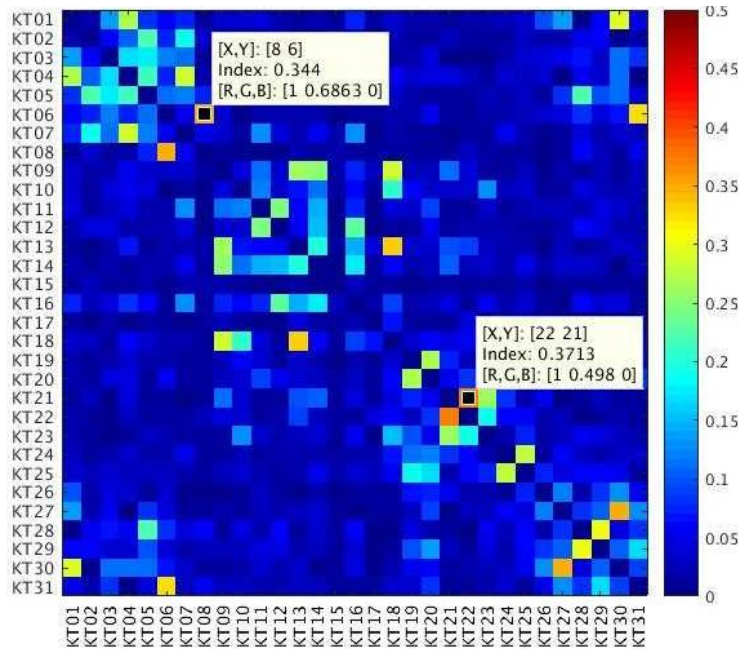


Figure 4 – Experimental noise correlation map for the 10.5-32Rx receiver demonstrating effective decoupling of receive elements. Maximum noise correlation is 0.37.

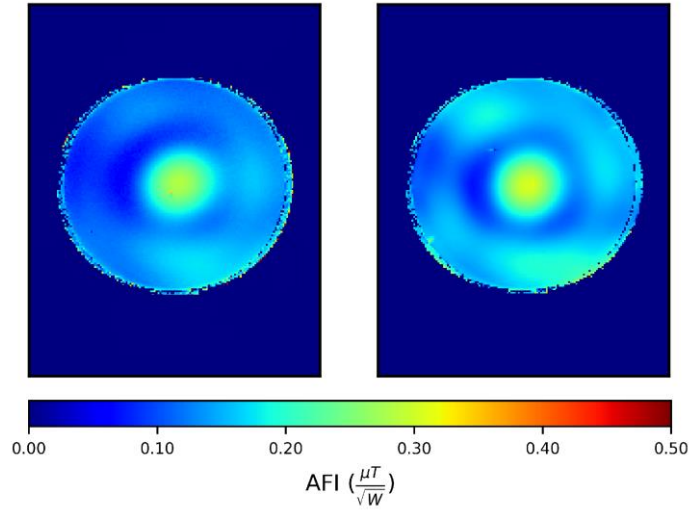


Figure 5 - Comparing experimental normalized transmit field maps of (left) 10.5T-16Tx used as transceiver without the presence of 32Rx versus (right) 10.5T-16Tx/32Rx demonstrating the effect of Rx insertion to be limited to  $\pm 10\%$  where signal intensity is reliable.

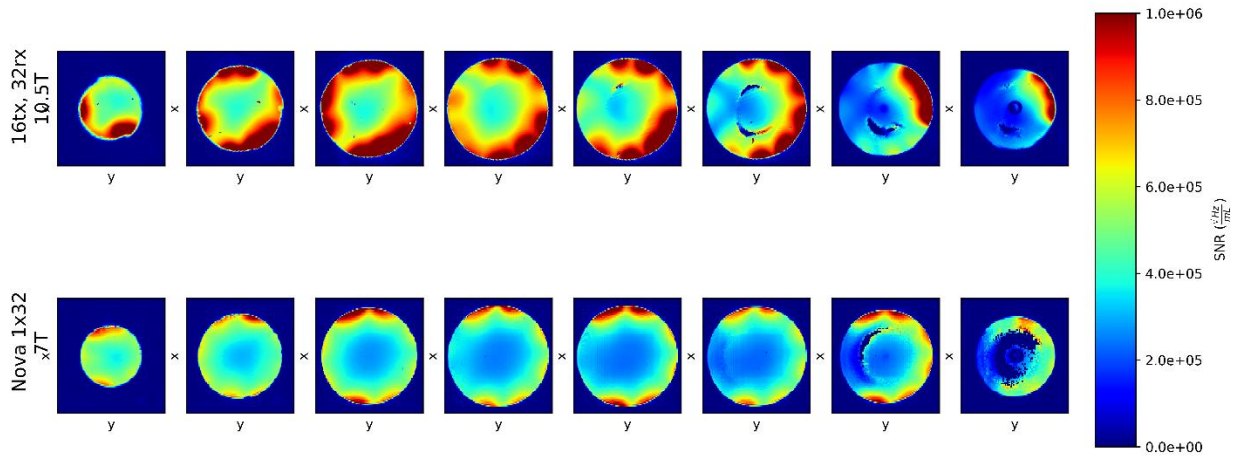


Figure 6 – Comparing normalized SNR of the 10.5T-32Rx (top row) and industry-standard 7T-32Rx (bottom row) on eight axial slices. Local defects (the crescent-shaped signal loss in first three slices from right) are due to specific transmit  $B_1^+$  shim. The dark center (in the first two slices from right) is an oil reference. Numbers in  $\sqrt{(Hz)}/ml$ .

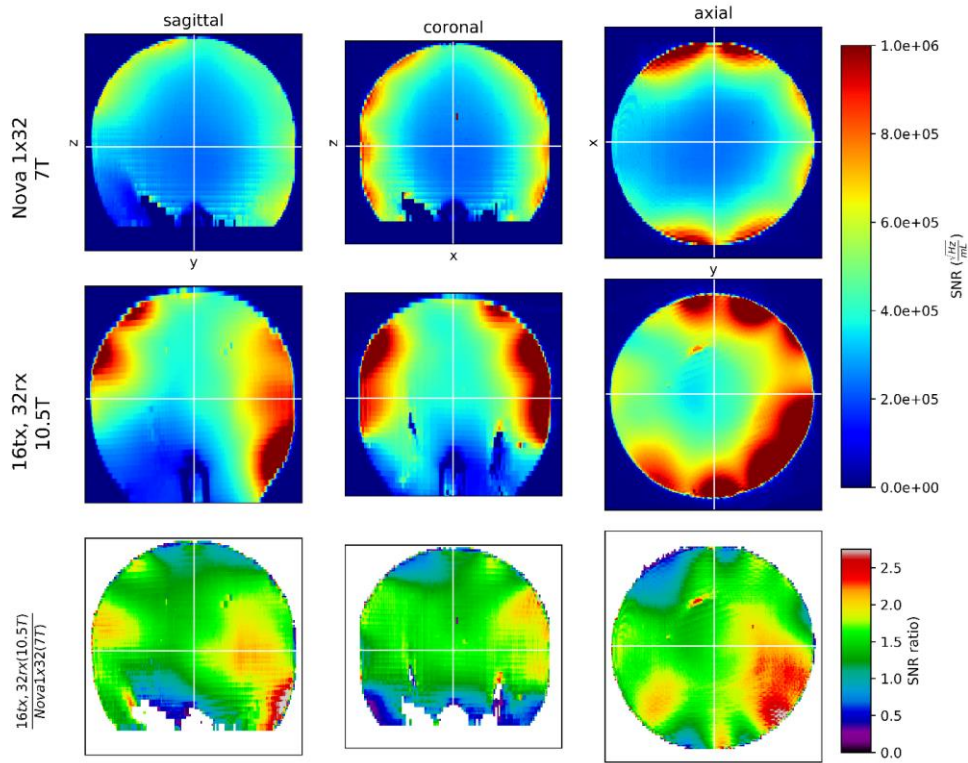


Figure 7 - Comparing SNR from the 7T-32Rx (top row) with SNR from 10.5T-32Rx (middle row) in three orthogonal planes, showing the map of ratio of 10.5T-32Rx SNR divided by 7T-32Rx SNR (bottom row).

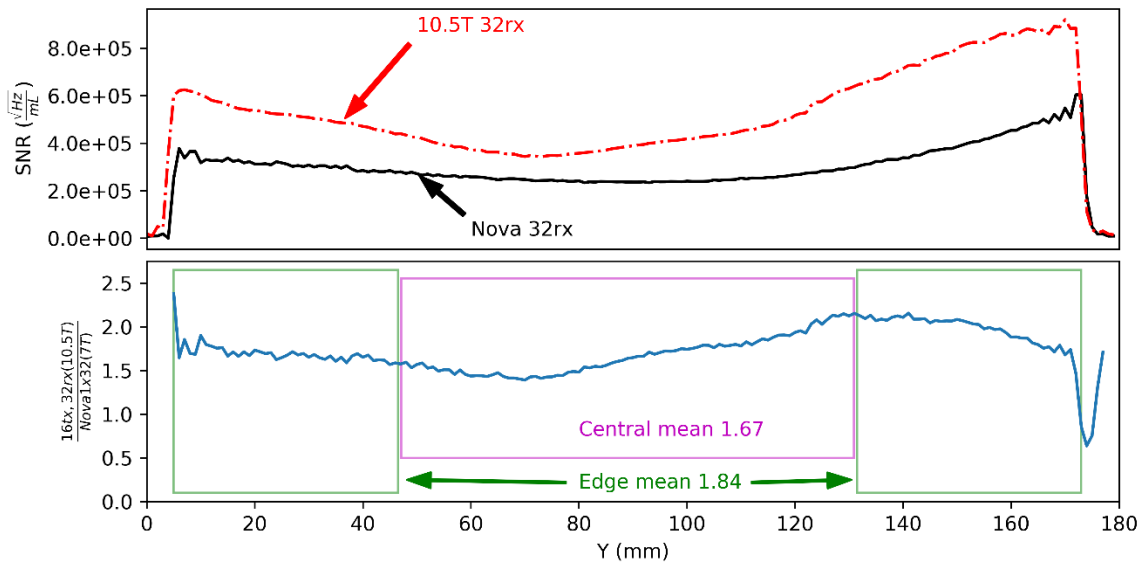


Figure 8 – Line plot of SNR comparing (top) SNR of the 10.5T-32Rx with 7T-32Rx, and (bottom) ratio of 10.5T-32Rx SNR divided by 7T-32Rx SNR along the y-axis in the central axial slice.

Loop size	SOM	RSOS	SNR
25x50 mm <sup>2</sup>	19	17	10
50x50 mm <sup>2</sup>	47	32	26

Table 1. Percentage increase in SOM, RSOS, and SNR obtained using self-decoupled loops instead of overlap-decoupled loops (i.e. (self\_decoupling – overlap)/overlap \* 100) at 10.5T/447MHz.

	g-factor		Inverse g-factor	
10.5T-32Rx	Mean	1.44	Mean	0.69
	Max	1.8	Min	0.56
7T-64Rx	Mean	1.3	Mean	0.77
	Max	1.9	Min	0.53
7T-32Rx	Mean	1.7	Mean	0.59
	Max	2.7	Min	0.37

Table 2 – Comparing g-factor values for 4x4 2D accelerated acquisitions using 10.5T-32Rx with g-factor values for 7T-64Rx and 7T-32Rx<sup>13</sup>.

## REFERENCES

1. Ladd ME, Bachert P, Meyerspeer M, et al. Pros and cons of ultra-high-field MRI/MRS for human application. *Prog Nucl Magn Reson Spectrosc.* 2018;109:1-50. doi:10.1016/J.PNMRS.2018.06.001
2. Uğurbil K. Imaging at ultrahigh magnetic fields: History, challenges, and solutions. *Neuroimage.* 2018;168:7-32. doi:10.1016/J.NEUROIMAGE.2017.07.007
3. Boyacıoğlu R, Schulz J, Müller NCJ, Koopmans PJ, Barth M, Norris DG. Whole brain, high resolution multiband spin-echo EPI fMRI at 7 T: A comparison with gradient-echo EPI using a color-word Stroop task. *Neuroimage.* 2014;97:142-150. doi:10.1016/J.NEUROIMAGE.2014.04.011
4. Uludağ K, Blinder P. Linking brain vascular physiology to hemodynamic response in ultra-high field MRI. *Neuroimage.* 2018;168:279-295. doi:10.1016/J.NEUROIMAGE.2017.02.063
5. Wu X, Auerbach EJ, Vu AT, et al. High-resolution whole-brain diffusion MRI at 7T using radiofrequency parallel transmission. *Magn Reson Med.* 2018;80(5):1857-1870. doi:10.1002/mrm.27189
6. Uğurbil K, Xu J, Auerbach EJ, et al. Pushing spatial and temporal resolution for functional and diffusion MRI in the Human Connectome Project. *Neuroimage.* 2013;80:80-104. doi:10.1016/J.NEUROIMAGE.2013.05.012
7. Gallichan D. Diffusion MRI of the human brain at ultra-high field (UHF): A review. *Neuroimage.* 2018;168:172-180. doi:10.1016/J.NEUROIMAGE.2017.04.037
8. De Martino F, Yacoub E, Kemper V, et al. The impact of ultra-high field MRI on cognitive and computational neuroimaging. *Neuroimage.* 2018;168(March):366-382. doi:10.1016/j.neuroimage.2017.03.060
9. Dumoulin SO, Fracasso A, van der Zwaag W, Siero JCW, Petridou N. Ultra-high field MRI: Advancing systems neuroscience towards mesoscopic human brain function. *Neuroimage.* 2018;168:345-357. doi:10.1016/j.neuroimage.2017.01.028
10. Polimeni JR, Uludağ K. Neuroimaging with ultra-high field MRI: Present and future. *Neuroimage.* 2018;168:1-6. doi:10.1016/j.neuroimage.2018.01.072
11. Trattnig S, Springer E, Bogner W, et al. Key clinical benefits of neuroimaging at 7T. *Neuroimage.* 2016;168(November):477-489. doi:10.1016/j.neuroimage.2016.11.031
12. Obusez EC, Lowe M, Oh S-H, et al. 7T MR of intracranial pathology: Preliminary observations and comparisons to 3T and 1.5T. *Neuroimage.* 2018;168:459-476. doi:10.1016/J.NEUROIMAGE.2016.11.030
13. Uğurbil K, Auerbach E, Moeller S, et al. Brain imaging with improved acceleration and SNR at 7 Tesla obtained with 64-channel receive array. *Magn Reson Med.* February 2019. doi:10.1002/mrm.27695
14. Sati P. Diagnosis of multiple sclerosis through the lens of ultra-high-field MRI. *J Magn Reson.* 2018;291:101-109. doi:10.1016/J.JMR.2018.01.022
15. Ocali O, Atalar E. Ultimate intrinsic signal-to-noise ratio in MRI. *Magn Reson Med.* 1998;39(3):462-473. doi:10.1002/mrm.1910390317
16. Schnell W, Renz W, Vester M, Ermert H. Ultimate signal-to-noise-ratio of surface and body antennas for magnetic resonance imaging. *IEEE Trans Antennas Propag.* 2000;48(3):418-428. doi:10.1109/8.841903
17. Schmitter S, Schnell S, Uğurbil K, et al. Towards high-resolution 4D flow MRI in the human aorta using kt-GRAPPA and B1+ shimming at 7T. *J Magn Reson Imaging.* 2016;44(2):486-499. doi:10.1002/jmri.25164
18. Arcan M, Urk E, Wu X, et al. Toward Imaging the Body at 10.5 Tesla. *Magn Reson Med.* 2017;77:434-443. doi:10.1002/mrm.26487
19. Wiesinger F, Van de Moortele P-F, Adriany G, De Zanche N, Uğurbil K, Pruessmann KP. Potential and feasibility of parallel MRI at high field. *NMR Biomed.* 2006;19(3):368-378. doi:10.1002/nbm.1050
20. Fiedler TM, Ladd ME, Bitz AK. SAR Simulations & Safety. *Neuroimage.* 2017;(March). doi:10.1016/j.neuroimage.2017.03.035
21. Setsompop K, Kimmlingen R, Eberlein E, et al. Pushing the limits of in vivo diffusion MRI for the Human Connectome Project. *Neuroimage.* 2013;80:220-233. doi:10.1016/J.NEUROIMAGE.2013.05.078
22. Ipek Ö. Radio-frequency coils for ultra-high field magnetic resonance. *Anal Biochem.* 2017;529:10-16. doi:10.1016/j.ab.2017.03.022
23. Van de Moortele P-FF, Akgun C, Adriany G, et al. B1 destructive interferences and spatial phase patterns at 7 T with a head transceiver array coil. *Magn Reson Med.* 2005;54(6):1503-1518. doi:10.1002/mrm.20708
24. Keil B, Wald LL. Massively parallel MRI detector arrays. *J Magn Reson.* 2013;229:75-89. doi:10.1016/j.jmr.2013.02.001
25. Vaidya M V., Sodickson DK, Lattanzi R. Approaching ultimate intrinsic SNR in a uniform spherical sample



- with finite arrays of loop coils. *Concepts Magn Reson Part B Magn Reson Eng.* 2014;44(3):53-65. doi:10.1002/cmr.b.21268
26. Ra JB, Rim CY. Fast imaging using subencoding data sets from multiple detectors. *Magn Reson Med.* 1993;30(1):142-145. doi:10.1002/mrm.1910300123
  27. Pruessmann KP, Weiger M, Scheidegger MB, Boesiger P. SENSE: Sensitivity encoding for fast MRI. *Magn Reson Med.* 1999;42(5):952-962. doi:10.1002/(SICI)1522-2594(199911)42:5<952::AID-MRM16>3.0.CO;2-S
  28. Wiesinger F, Van de Moortele P-F, Adriany G, De Zanche N, Ugurbil K, Pruessmann KP. Parallel imaging performance as a function of field strength - An experimental investigation using electrodynamic scaling. *Magn Reson Med.* 2004;52(5):953-964. doi:10.1002/mrm.20281
  29. Aja-Fernández S, Vegas-Sánchez-Ferrero G, Tristán-Vega A. Noise estimation in parallel MRI: GRAPPA and SENSE. *Magn Reson Imaging.* 2014;32(3):281-290. doi:10.1016/j.mri.2013.12.001
  30. Breuer FA, Kannengiesser SAR, Blaimer M, Seiberlich N, Jakob PM, Griswold MA. General formulation for quantitative G-factor calculation in GRAPPA reconstructions. *Magn Reson Med.* 2009;62(3):739-746. doi:10.1002/mrm.22066
  31. Keil B. Construction of Receive Arrays. *Proc Intl Soc Mag Reson Med.* 2013;21:1-10.
  32. Wiggins GC, Polimeni JR, Potthast A, Schmitt M, Alagappan V, Wald LL. 96-Channel receive-only head coil for 3 Tesla: Design optimization and evaluation. *Magn Reson Med.* 2009;62(3):754-762. doi:10.1002/mrm.22028
  33. Keil B, Blau JN, Biber S, et al. A 64-channel 3T array coil for accelerated brain MRI. *Magn Reson Med.* 2013;70(1):248-258. doi:10.1002/mrm.24427
  34. Vaughan TJ, Griffiths JR, eds. *RF Coils for MRI.* 1st ed. John Wiley & Sons Ltd; 2012.
  35. Roemer PB, Edelstein WA, Hayes CE, Souza SP, Mueller OM. The NMR phased array. *Magn Reson Med.* 1990;16(2):192-225. doi:10.1002/mrm.1910160203
  36. Shajan G, Hoffmann J, Adriany G, Ugurbil K, Scheffler K. A 7T Head Coil with 16-channel dual-row transmit and 31-channel receive for pTx applications. In: *24th Annual Meeting and Exhibition of the International Society for Magnetic Resonance in Medicine.* ; 2016. <http://archive.ismrm.org/2016/2132.html>.
  37. Shajan G, Kozlov M, Hoffmann J, Turner R, Scheffler K, Pohmann R. A 16-channel dual-row transmit array in combination with a 31-element receive array for human brain imaging at 9.4 T. *Magn Reson Med.* 2014;71(2):870-879. doi:10.1002/mrm.24726
  38. Wiggins GC, Triantafyllou C, Potthast A, Reykowski A, Nittka M, Wald LL. 32-channel 3 Tesla receive-only phased-array head coil with soccer-ball element geometry. *Magn Reson Med.* 2006;56(1):216-223. doi:10.1002/mrm.20925
  39. Cohen-Adad J, Mareyam A, Keil B, Polimeni JR, Wald LL. 32-Channel RF coil optimized for brain and cervical spinal cord at 3 T. *Magn Reson Med.* 2011;66(4):1198-1208. doi:10.1002/mrm.22906
  40. Yan X, Gore JC, Grissom WA. Self-decoupled radiofrequency coils for magnetic resonance imaging. *Nat Commun.* 2018;9(1):3481. doi:10.1038/s41467-018-05585-8
  41. Lakshmanan K, Cloos M, Lattanzi R, Sodickson D, Wiggins G. The Loopole Antenna: Capturing Magnetic and Electric Dipole Fields with a Single Structure to Improve Transmit and Receive Performance. *Proc Intl Soc Mag Reson Med* 22. 2014:0397. <https://cds.ismrm.org/protected/14MProceedings/files/0397.pdf>. Accessed March 23, 2019.
  42. Lee RF, Giaquinto RO, Hardy CJ. Coupling and decoupling theory and its application to the MRI phased array. *Magn Reson Med.* 2002;48(1):203-213. doi:10.1002/mrm.10186
  43. Zhang X, Webb A. Design of a capacitively decoupled transmit/receive NMR phased array for high field microscopy at 14.1 T. *J Magn Reson.* 2004;170(1):149-155. doi:10.1016/j.jmr.2004.05.004
  44. Tavaf N, Lagore RL, Jungst S, et al. Developing High Channel Count Receive Arrays for Human Brain Imaging at 10.5T. *Int Soc Magn Reson Med.* 2020.
  45. Adriany G, Radder J, Tavaf N, et al. Evaluation of a 16-Channel Transmitter for Head Imaging at 10.5T. In: *2019 International Conference on Electromagnetics in Advanced Applications (ICEAA).* IEEE; 2019:1171-1174. doi:10.1109/ICEAA.2019.8879131
  46. Hasgall P, Di Gennaro F, Baumgartner C, et al. IT'IS Database for thermal and electromagnetic parameters of biological tissues. *ITIS Database.* 2018:Version 4.0. doi:10.13099/VIP21000-04-0
  47. Robson PM, Grant AK, Madhuranthakam AJ, Lattanzi R, Sodickson DK, McKenzie CA. Comprehensive quantification of signal-to-noise ratio and g -factor for image-based and k -space-based parallel imaging reconstructions. *Magn Reson Med.* 2008;60(4):895-907. doi:10.1002/mrm.21728
  48. Kellman P, McVeigh ER. Image reconstruction in SNR units: A general method for SNR measurement.

- Magn Reson Med.* 2005;54(6):1439-1447. doi:10.1002/mrm.20713
49. Wiesinger F, Boesiger P, Pruessmann KP. Electrodynamics and ultimate SNR in parallel MR imaging. *Magn Reson Med.* 2004;52(2):376-390. doi:10.1002/mrm.20183
  50. Wang J. Relation between noise correlation and transmission coefficient of surface coils for magnetic resonance imaging. In: *Proceedings of 17th International Conference of the Engineering in Medicine and Biology Society.* Vol 1. IEEE; 1993:469-470. doi:10.1109/IEMBS.1995.575204
  51. Tavaf N, Lagore RL, Moen S, et al. A 15-channel loop dipole array for in-vivo swine head MR imaging at 10.5T. In: *International Society of Magnetic Resonance in Medicine.* Vol 27. ; 2019:1445. <https://index.mirasmart.com/ISMRM2019/PDFfiles/1445.html>.
  52. Seeber DA, Jevtic J, Menon A. Floating shield current suppression trap. *Concepts Magn Reson.* 2004;21B(1):26-31. doi:10.1002/cmr.b.20008
  53. Brown J, Whitlock B. Common-Mode to Differential-Mode Conversion in Shielded Twisted-Pair Cables (Shield-Current-Induced Noise). *114th AES Conv Amsterdam.* 2003:5747. <http://www.aes.org/e-lib/>. Accessed June 17, 2019.
  54. Van de Moortele PF, Snyder C, DelaBarre L, Adriany G, Vaughan T, Ugurbil K. Calibration Tools for RF Shim at Very High Field with Multiple Element RF Coils : from Ultra Fast Local Relative Phase to Absolute Magnitude B1+ Mapping. *Proc Intl Soc Mag Reson Med 15.* 2007:1676.
  55. Adriany G, Van De Moortele P-FF, Wiesinger F, et al. Transmit and receive transmission line arrays for 7 tesla parallel imaging. *Magn Reson Med.* 2005;53(2):434-445. doi:10.1002/mrm.20321
  56. Yarnykh VL. Actual flip-angle imaging in the pulsed steady state: A method for rapid three-dimensional mapping of the transmitted radiofrequency field. *Magn Reson Med.* 2007;57(1):192-200. doi:10.1002/mrm.21120
  57. Van de Moortele P, Snyder C, DelaBarre L, Vaughan J, Ugurbil K. Shimming at Very High Field with Multiple Element RF Coils: Calibration Tools from Ultra Fast Local Relative B1+/- Phase to Absolute Magnitude B1+ Mapping. In: *International Society of Magnetic Resonance in Medicine.* ; 2007:1676.
  58. Van de Moortele P-F, Ugurbil K. Very fast multi channel B1 calibration at high field in the small flip angle regime. In: *International Society of Magnetic Resonance in Medicine.* ; 2009:367.
  59. NEMA. Determination of Signal-to-Noise Ratio (SNR) in Diagnostic Magnetic Resonance Imaging. In: *NEMA Standards Publication MS 1-2008 (R2014).* ; 2008. [www.nema.org](http://www.nema.org). Accessed June 12, 2020.
  60. Ellermann J, Goerke U, Morgan P, et al. Simultaneous bilateral hip joint imaging at 7 Tesla using fast transmit B1 shimming methods and multichannel transmission - a feasibility study. *NMR Biomed.* 2012;25(10):1202-1208. doi:10.1002/nbm.2779
  61. J. W. Radder, S. Moeller, G. Adriany, et al. Simulation of B1 efficiency in 64-channel phased head arrays at 7T and 10.5T. *Proc Intl Soc Mag Reson Med.* 2017;25(3):4285. <http://cds.ismrm.org/protected/17MPresentations/abstracts/4285.html>.
  62. Pohmann R, Speck O, Scheffler K. Signal-to-noise ratio and MR tissue parameters in human brain imaging at 3, 7, and 9.4 tesla using current receive coil arrays. *Magn Reson Med.* 2016;75(2):801-809. doi:10.1002/mrm.25677
  63. Guérin B, Villena JF, Polimeridis AG, et al. The ultimate signal-to-noise ratio in realistic body models. *Magn Reson Med.* 2017;78(5):1969-1980. doi:10.1002/mrm.26564
  64. Pfrommer A, Henning A. The ultimate intrinsic signal-to-noise ratio of loop- and dipole-like current patterns in a realistic human head model. *Magn Reson Med.* 2018;80(5):2122-2138. doi:10.1002/mrm.27169
  65. Wiesinger F, Boesiger P, Pruessmann KP. Electrodynamics and ultimate SNR in parallel MR imaging. *Magn Reson Med.* 2004;52(2):376-390. doi:10.1002/mrm.20183